Facile synthesis of high-quality graphene nanoribbons

Liying Jiao, Xinran Wang, Georgi Diankov, Hailiang Wang and Hongjie Dai*

Graphene nanoribbons have attracted attention because of their novel electronic and spin transport properties[1-6], and also because nanoribbons less than 10 nm wide have a bandgap that can be used to make field-effect transistors[1-3]. However, producing nanoribbons of very high quality, or in high volumes, remains a challenge[1,4-18]. Here, we show that pristine few-layer nanoribbons can be produced by unzipping mildly gas-phase oxidized multiwalled carbon nanotubes using mechanical sonication in an organic solvent. The nanoribbons are of very high quality, with smooth edges (as seen by high-resolution transmission electron microscopy), low ratios of disorder to graphitic Raman bands, and the highest electrical conductance and mobility reported so far (up to $5e^2/h$ and 1,500 cm^2 V^{-1} s^{-1} for ribbons 10–20 nm in width). Furthermore, at low temperatures, the nanoribbons show phase-coherent transport and Fabry–Perot interference, suggesting minimal defects and edge roughness. The yield of nanoribbons is ∼2% of the starting raw nanotube soot material, significantly higher than previous methods capable of producing high-quality narrow nanoribbons[1]. The relatively high-yield synthesis of pristine graphene nanoribbons will make these materials easily accessible for a wide range of fundamental and practical applications.

Lithographic[4,5,7], chemical[8-11] and sonochemical[1,12] methods have been developed to make graphene nanoribbons and, recently, nanoribbon formation has been achieved by unzipping carbon nanotubes[13-18]. Two groups have successfully unzipped multiwalled carbon nanotubes (MWNTs; grown by chemical vapour deposition, CVD) in the solution phase by using potassium permanganate oxidation[14] and lithium and ammonia reactions[16], respectively. However, only heavily oxidized and defective nanoribbons were obtained owing to the extensive oxidation involved in the unzipping process. We have previously developed an approach to fabricate high-quality, narrow nanoribbons by unzipping nanotubes using a masked gas-phase plasma etching approach[13]. However, that method was limited to the formation of nanoribbons on substrates. More recently, unzipping methods such as catalytic cutting[17] and high-current pulse burning[18] have been reported, but the resultant quality and yield of nanoribbons are unknown. Thus far, a method capable of producing large amounts of high-quality nanoribbons is still lacking.
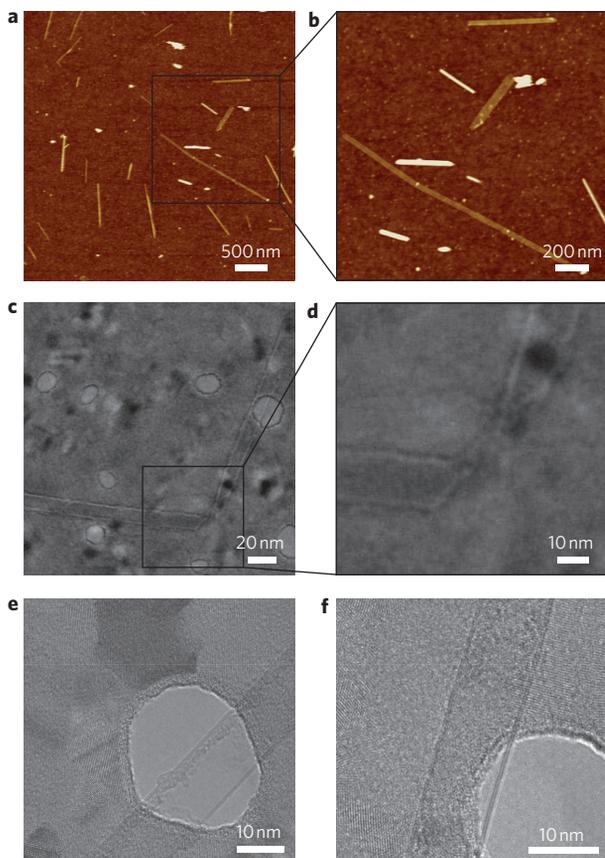
Here, we present a new method to unzip nanotubes using a simple two-step process (Fig. 1a). Raw soot materials containing pristine MWNTs synthesized by arc discharge (Bucky tube, Aldrich) were first calcined in air at 500 °C. This is a mild condition known to remove impurities and etch/oxidize MWNTs at defect sites and ends without oxidizing the pristine sidewalls of the nanotubes[19]. The nanotubes were then dispersed in a 1,2-dichloroethane (DCE) organic solution of poly(m-phenylenevinylene-co-2,5-dioctoxy-p-phenylenevinylene) (PmPV) by sonication, during which the calcined nanotubes were found to unzip into

nanoribbons with high efficiency. An ultracentrifuge step was then applied to remove the remaining nanotubes and graphitic carbon nanoparticles, resulting in high percentage (>60%) of nanoribbons in the supernatant (Supplementary Fig. S1). The yield of nanoribbons was estimated to be ∼2% of the starting raw nanotube soot material using this two-step process, which could be further improved by repeating the unzipping procedure for the nanotubes remaining in the centrifuged aggregate, increasing the calcination temperature, and prolonging the sonication time. The yield and quantity of high-quality nanoribbons (width 10–30 nm) far exceeds those of previous methods capable of producing high-quality narrow ribbons[1,13].

We used atomic force microscopy (AFM) to characterize the MWNTs and the unzipped products deposited on SiO$_2$/silicon substrates. Nanoribbons were easily distinguished from the MWNTs because of their obviously smaller apparent heights (heights of 1–2.5 nm for nanoribbons, Fig. 1b–d; see also Supplementary
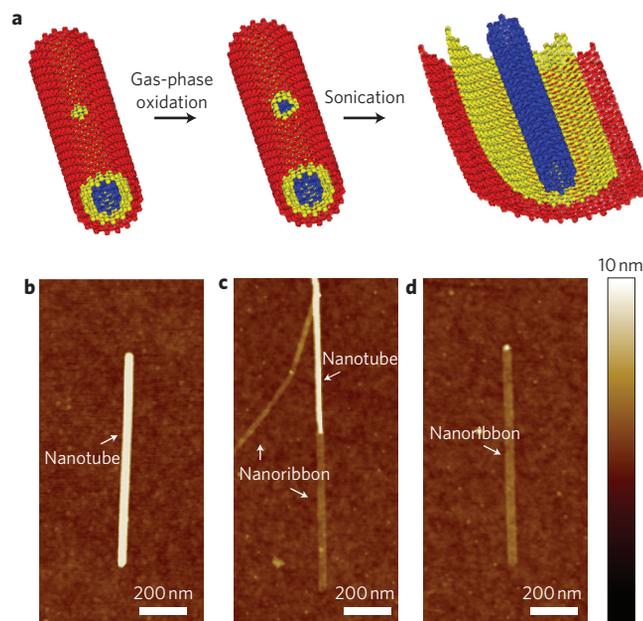

Figure 1 | Unzipping of nanotubes using a new two-step method in gas and liquid phases. a, Schematic of the unzipping processes. In the mild gas-phase oxidation step, oxygen reacts with pre-existing defects on nanotubes to form etch pits on the sidewalls. In the solution-phase sonication step, sonochemistry and hot gas bubbles enlarge the pits and unzip the tubes. **b–d,** AFM images of pristine, partially and fully unzipped nanotubes, respectively. The heights of the nanoribbons in **c** and **d** are 1.4 and 1.6 nm, respectively, much lower than the pristine nanotube shown in **b** (height ∼9 nm).

Department of Chemistry and Laboratory for Advanced Materials, Stanford University, Stanford, California 94305, USA. *e-mail: hdai@stanford.edu

Figure 2 | Microscopy imaging of nanoribbons. a, AFM image of unzipped nanotubes deposited on a SiO$_2$/silicon substrate, showing a high percentage of single-, bi- and trilayer nanoribbons. **b**, Enlarged AFM image of the area marked in **a**, showing the smooth edges of the nanoribbons. Heights and widths of the three nanoribbons, from top to bottom: 1.8 nm, 18 nm; 1.4 nm, 48 nm; 1.4 nm, 22 nm, respectively. **c**, TEM (acceleration voltage = 200 kV) image of a ~12-nm-wide nanoribbon with a kink due to folding. The dark spots on the substrate are nanocrystalline domains within the porous silicon grids. **d**, TEM image of the kink on the nanoribbon shown in **c. e,f**, TEM (acceleration voltage = 120 kV) images of nanoribbons suspended over the holes of porous silicon grids, showing nearly atomically smooth edges. The widths of the nanoribbons in **e** and **f** were ~12 and 10 nm, respectively. The amorphous coating on the nanoribbon shown in **e** is the PmPV used to suspend nanoribbons.

Fig. S2), the average diameter (height) of the starting nanotubes being ~8 nm. From the topographic heights of the nanoribbons (1–2.5 nm, including PmPV on both sides of the ribbons), it was observed that most of the ribbons were either single-, bi- or trilayered, with widths in the range 10–30 nm (Fig. 2a,b; see also Supplementary Figs S2,S3). Under AFM, the nanoribbons appeared to be very uniform in width, with little edge roughness along their lengths (Fig. 2b; Supplementary Fig. S3). The high yield of nanoribbons enabled us to readily characterize them by transmission electron microscopy (TEM) (which was not the case in ref. 1). Using TEM we observed a ~12-nm-wide nanoribbon with a fold along its length (Fig. 2c). The kink structure (Fig. 2d) illustrated the excellent flexibility of nanoribbons when compared with rigid MWNTs. High-resolution TEM of our nanoribbons revealed straight and nearly atomically smooth edges without any discernable edge roughness (Fig. 2e,f; Supplementary Fig. S4). This is the first time that nearly atomically smooth edges of narrow (<20 nm) nanoribbons have been observed using TEM. The parallel lines seen at the edges of the nanoribbon (Fig. 2e,f; inter-line
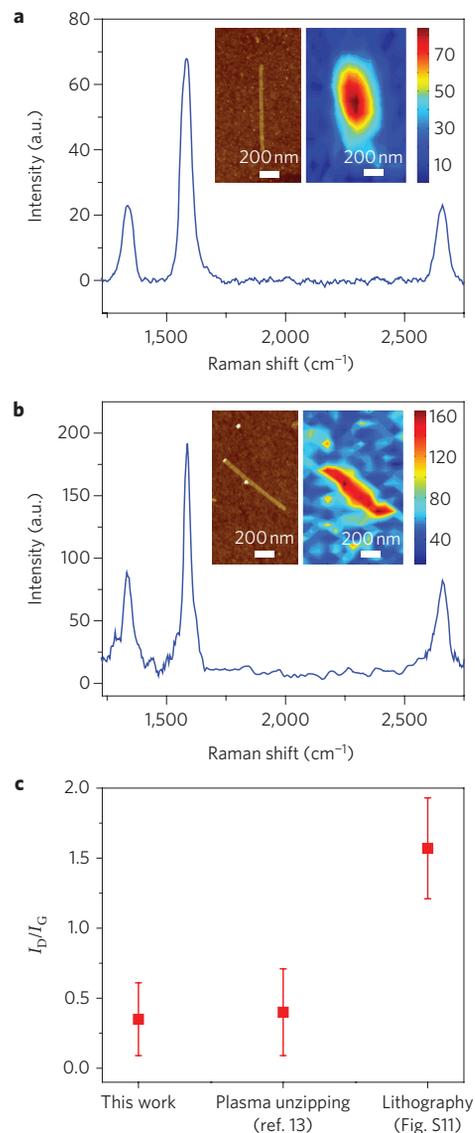
Figure 3 | Raman spectroscopy of nanoribbons. a,b, Raman spectra of bilayer (**a**, height ≈ 1.5 nm) and trilayer (**b**, height ≈ 1.8 nm) nanoribbons ($W \approx 20$ nm) on SiO$_2$/silicon substrates. Insets: AFM (left) and G-band (right) images of the same nanoribbons on the same length scale. The I_D/I_G ratios of these two nanoribbons are 0.3 and 0.5, respectively. **c**, Comparison of averaged I_D/I_G of 5–10 bilayer nanoribbons with ~20 nm widths made by different methods, including the method present in this paper, lithographic patterning (Supplementary Fig. S11) and plasma unzipping[13].

spacing of 3.7–4 Å) could indicate that this is a bilayer nanoribbon, with the successively smaller widths of each layer being due to the decreasing circumference of the inner nanotube shells.

Our method produced a high percentage of nanoribbons with ultra-smooth edges by means of simple calcination and sonication steps, which can be performed in many laboratories. The mechanism of the unzipping process differs from a previous method, which involved extensive solution-phase oxidation[14]. We propose that our calcination step led to gas-phase oxidation of pre-existing defects existing on arc-discharge-grown MWNTs. A low-density structural defect is known to exist on the sidewalls and the ends of high-quality arc-derived MWNTs[19]. These defects and ends were more reactive with oxygen than the pristine sidewalls during calcination at 500 °C, a condition used for purifying arc-discharge MWNTs without introducing new defects on the sidewalls[19,20]. In a manner
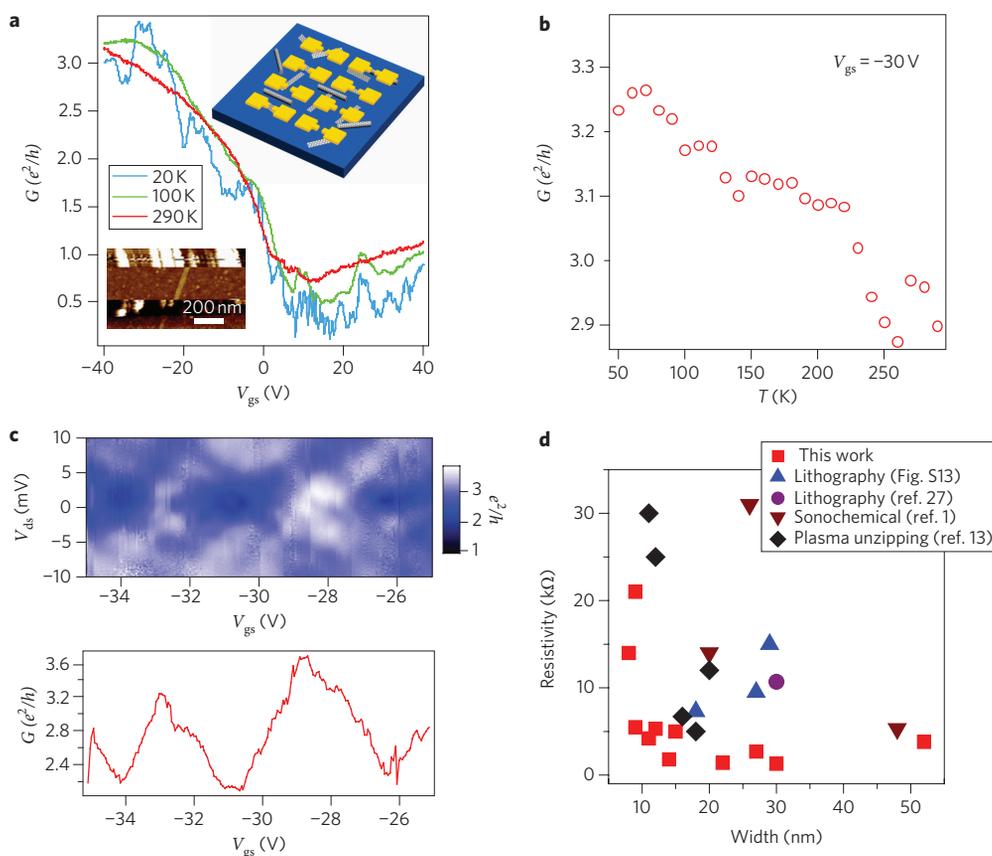
Figure 4 | Electrical transport measurements of nanoribbons. a, G–V_{gs} curves of a 14-nm-wide bilayer nanoribbon at 20, 100 and 290 K ($V_{ds} = 1$ mV). Upper inset: schematic of nanoribbon devices made by randomly contacting. Lower inset: AFM image of this nanoribbon device. **b**, G–T relationship of the nanoribbon shown in **a** at V_{gs} of −30 V. The conductance increased as the device was cooled from room temperature to 50 K. **c**, Top panel: differential conductance dI_{ds}/dV_{ds} versus V_{ds} and V_{gs} of the nanoribbon shown in **a** measured in a cryogenic insert at 4.2 K shows a Fabry–Perot-like interference pattern. Bottom panel: the dI_{ds}/dV_{ds} versus V_{gs} curve of the nanoribbon shown in **a** at $V_{ds} = 0$ mV shows conductance peaks and valleys. **d**, Comparison of room-temperature resistivity of bilayer nanoribbons of 10–30 nm widths made by different methods, including the method present in this paper, lithographic patterning[27] (Supplementary Fig. S13), a sonochemical method[1] and plasma unzipping[13]. The resistivity ($\sim$1 MΩ) of wide nanoribbons made by unzipping nanotubes in the solution phase[14,15] was not included in the comparison.

similar to the oxidation of defects in the plane of graphite by oxygen[21,22], etch pits were formed at the defects and extended from the outmost sidewall into adjacent inner walls. The depth of pits formed in this step determined the number of layers of the resulting nanoribbons. Most of our nanoribbons were single-, bi- or trilayers, suggesting the formation of etch pits through 1–3 walls on nanotubes during the calcination step. The oxidation condition was relatively mild, and did not create new defects or functional groups in the nanotubes, as was made evident by the low Raman D-band intensity and the fact that the oxygen level measured by X-ray photoelectron spectroscopy (XPS) was similar to that of pristine MWNTs (Supplementary Figs S5,S6). In the solution-phase sonication process, sonochemistry and hot gas bubbles created during sonication caused unzipping, which was initiated at the weak points of etch pits on the nanotubes and proceeded along the tube axis. The resulting nanoribbons were separated from the inner tubes and noncovalently functionalized by PmPV by means of π-stacking[1,23] to afford a homogeneous suspension in DCE. Scanning electron microscopy (SEM) imaging of pristine, calcined and sonicated nanotubes after calcination also indicated that unzipping of nanotubes occurred during the sonication step (Supplementary Fig. S7). We carried out various control experiments (Supplementary Figs S8,S9), which led to an optimized unzipping protocol (see Methods). Note that our unzipping process was also applicable to CVD-grown MWNTs (Supplementary Fig. S10).

We characterized our materials by means of Raman spectroscopy. The Raman I_D/I_G ratio (where I_D and I_G are the D-band and G-band Raman intensities, respectively) is widely used to evaluate the quality of carbon nanotubes[24] and graphene materials[25]. The I_D/I_G ratio of nanoribbons is related to density of defects in the ribbon, as well as edge smoothness and edge structures (that is, armchair and zig-zag)[26]. However, because the edge structures of the experimentally made nanoribbons are unknown as yet, and could be random, the averaged I_D/I_G may reflect the quality of the nanoribbons (including edge quality; for example, edge roughness and defects) with the same width and number of layers. The ensemble-averaged I_D/I_G ratio of our final bulk product containing $\sim$60% nanoribbons was only $\sim$0.2 (Supplementary Fig. S5), similar to that of the starting pristine nanotubes, and suggested an overall low defect density in the product. We also carried out conformal Raman mapping of individual bi- and trilayer nanoribbons deposited on SiO$_2$/silicon substrates (Fig. 3a,b). The averaged I_D/I_G ratio of nanoribbons with widths of $\sim$20 nm was $\sim$0.4 (Fig. 3c), much lower than lithographic patterned nanoribbons with similar widths ($I_D/I_G \approx 1.5$; Supplementary Fig. S11) and wide nanoribbons unzipped by solution-phase oxidation ($I_D/I_G > 1$)[14,15].

The high yield of nanoribbons suspended in an organic solution greatly simplifies the fabrication of nanoribbon electrical devices. We fabricated field-effect transistor (FET)-like nanoribbon devices by simply constructing a large array of source and drain electrodes

arranged to contact randomly deposited nanoribbons on SiO_2 (300 nm)/p^{++}-Si substrates and obtained ~15% single nanoribbon devices (Fig. 4a, upper inset). The p^{++}-Si was used as the back gate and palladium (thickness ~ 30 nm) was used as the source and drain electrodes. Electrical annealing in vacuum was used[3,13] to remove adsorbates from the nanoribbons by applying a bias voltage of ~2 V. The source–drain current/gate voltage (I_{ds}–V_{gs}) curves for most of the nanoribbons devices showed clear Dirac points at ~0 V after electrical annealing (Supplementary Fig. S12), and the individual nanoribbons showed a conductance of 0.5–5e^2/h at room temperature. The lowest resistivity (defined as $R \times W/L$, where R is the resistance of the device and W and L indicate the width and channel length of the nanoribbon, respectively) at the Dirac point observed in our nanoribbons (with widths of 10–30 nm) was 1.6 kΩ. This is the lowest resistivity of nanoribbons ever reported for nanoribbons with similar numbers of layers (1–3)[1,13,14,27] (Fig. 4d; Supplementary Fig. S13). The nanoribbons showed mobilities up to 1,500 cm^2 V^{-1} s^{-1} for ribbons with a width of only ~14 nm, based on a gate capacitance calculated by finite element modelling. This is the highest mobility reported for nanoribbons of similar widths[2,27]. The lowest resistivity and highest mobility values confirm the high quality of the nanoribbons produced by this new method.

Assessment of variable-temperature electrical transport in nanoribbons showed that conductance of the p-channel of a bilayer nanoribbon ($W \approx 14$ nm, $L \approx 200$ nm) increased as the device was cooled from 290 to 50 K (Fig. 4a,b; further cooling introduced some oscillations in the conductance/gate voltage (G–V_{gs}) characteristics). This suggested metallic behaviour for transport in the valence band of the narrow nanoribbon, with reduced acoustic phonon scattering at lower temperatures. Carrier scattering in our high-quality, smooth-edged nanoribbons was not dominated by defects, charged impurities or edge roughness, as is the case for nanoribbons obtained by lithographic patterning, which show increased resistance at lower temperatures due to localization effects of defects[5,28]. At 4.2 K, the conductance of our device, $G \approx 3$–4e^2/h, is at least one order of magnitude higher than similar nanoribbon devices fabricated previously. Conductance oscillations versus V_{gs} were recorded at 4.2 K, and differential conductance dI_{ds}/dV_{ds} versus V_{gs} and V_{ds} (where V_{ds} is the source–drain bias voltage) showed an interference pattern with peak conductance ~4e^2/h (Fig. 4c). This was similar to the Fabry–Perot interference previously observed in pristine carbon nanotubes[29], suggesting phase-coherent transport and interference of several modes or sub-bands of electrons in the nanoribbon. A similar interference pattern was only observed in a much wider and shorter graphene sample[30]. It is remarkable that electron waves travel ~200 nm in an open-edged narrow nanoribbon ($W \approx 14$ nm) without loss of phase coherence. The high conductance and phase-coherent transport in the valence band of our nanoribbons again confirmed the high quality of nanoribbons made using our new approach and the transparent contacts between the valence band of the nanoribbons and palladium. On the other hand, the conductance of the n-channel of our nanoribbons gradually decreased at lower temperatures, indicating a barrier for transport through the conduction band. This barrier is probably due to a small Schottky barrier between palladium and the conduction band of the $W \approx 14$ nm nanoribbon. The bandgap of the nanoribbon was estimated to be $E_g \approx 10$–15 meV by fitting the temperature dependence of minimum conductance to thermal activation over a barrier of ~$E_g/2$ (ref. 4).

In summary, we have developed a simple unzipping approach for production of pristine nanoribbons from MWNTs. For the first time, narrow nanoribbons showing nearly atomically smooth edges, a high conductance of up to 5e^2/h and phase-coherent transport have been obtained. This simple and reliable approach makes nanoribbons easily accessible for addressing many fundamental properties predicted for these materials and for exploring their potential applications. Besides promising applications in nanoelectronics, the availability of such high-quality nanoribbons also opens up new avenues to control the edge chemistry of graphene nanoribbons and for the production of nanoribbon–polymer composites covalently linked at the edges.

Methods

References

1. Li, X. L. *et al.* Chemically derived, ultrasmooth graphene nanoribbon semiconductors. *Science* **319,** 1229–1232 (2008).
2. Wang, X. R. *et al.* Room-temperature all-semiconducting sub-10-nm graphene nanoribbon field-effect transistors. *Phys. Rev. Lett.* **100,** 206803 (2008).
3. Wang, X. R. *et al.* N-doping of graphene through electrothermal reactions with ammonia. *Science* **324,** 768–771 (2009).
4. Chen, Z. H., Lin, Y. M., Rooks, M. J. & Avouris, P. Graphene nano-ribbon electronics. *Physica E* **40,** 228–232 (2007).
5. Han, M. Y., Ozyilmaz, B., Zhang, Y. B. & Kim, P. Energy band-gap engineering of graphene nanoribbons. *Phys. Rev. Lett.* **98,** 206805 (2007).
6. Cresti, A. *et al.* Charge transport in disordered graphene-based low dimensional materials. *Nano Res.* **1,** 361–394 (2008).
7. Tapaszto, L., Dobrik, G., Lambin, P. & Biro, L. P. Tailoring the atomic structure of graphene nanoribbons by scanning tunnelling microscope lithography. *Nature Nanotechnol.* **3,** 397–401 (2008).
8. Datta, S. S., Strachan, D. R., Khamis, S. M. & Johnson, A. T. C. Crystallographic etching of few-layer graphene. *Nano Lett.* **8,** 1912–1915 (2008).
9. Ci, L. J. *et al.* Controlled nanocutting of graphene. *Nano Res.* **1,** 116–122 (2008).
10. Campos, L. C., Manfrinato, V. R., Sanchez-Yamagishi, J. D., Kong, J. & Jarillo-Herrero, P. Anisotropic etching and nanoribbon formation in single-layer graphene. *Nano Lett.* **9,** 2600–2604 (2009).
11. Campos-Delgado, J. *et al.* Bulk production of a new form of sp^2 carbon: crystalline graphene nanoribbons. *Nano Lett.* **8,** 2773–2778 (2008).
12. Wu, Z. S. *et al.* Efficient synthesis of graphene nanoribbons sonochemically cut from graphene sheets. *Nano Res.* **3,** 16–22 (2010).
13. Jiao, L. Y., Zhang, L., Wang, X. R., Diankov, G. & Dai, H. J. Narrow graphene nanoribbons from carbon nanotubes. *Nature* **458,** 877–880 (2009).
14. Kosynkin, D. V. *et al.* Longitudinal unzipping of carbon nanotubes to form graphene nanoribbons. *Nature* **458,** 872–876 (2009).

15. Zhang, Z. X., Sun, Z. Z., Yao, J., Kosynkin, D. V. & Tour, J. M. Transforming carbon nanotube devices into nanoribbon devices. *J. Am. Chem. Soc.* **131,** 13460–13463 (2009).

16. Cano-Marquez, A. G. *et al.* Ex-MWNTs: graphene sheets and ribbons produced by lithium intercalation and exfoliation of carbon nanotubes. *Nano Lett.* **9,** 1527–1533 (2009).

17. Elías, A. L. *et al.* Longitudinal cutting of pure and doped carbon nanotubes to form graphitic nanoribbons using metal clusters as nanoscalpels. *Nano Lett.* **10,** 366–372 (2010).

18. Kim, W. S. *et al.* Fabrication of graphene layers from multiwalled carbon nanotubes using high d.c. pulse. *Appl. Phys. Lett.* **95,** 083103 (2009).

19. Colbert, D. T. *et al.* Growth and sintering of fullerene nanotubes. *Science* **266,** 1218–1222 (1994).

20. Barinov, A., Gregoratti, L., Dudin, P., La Rosa, S. & Kiskinova, M. Imaging and spectroscopy of multiwalled carbon nanotubes during oxidation: defects and oxygen bonding. *Adv. Mater.* **21,** 1916–1920 (2009).

21. Stevens, F., Kolodny, L. A. & Beebe, T. P. Kinetics of graphite oxidation: monolayer and multilayer etch pits in HOPG studied by STM. *J. Phys. Chem. B* **102,** 10799–10804 (1998).

22. Lee, S. M. *et al.* Defected-induced oxidation of graphite. *Phys. Rev. Lett.* **82,** 217–220 (1999).

23. Chen, R. J., Zhang, Y. G., Wang, D. W. & Dai, H. J. Noncovalent sidewall functionalization of single-walled carbon nanotubes for protein immobilization. *J. Am. Chem. Soc.* **123,** 3838–3839 (2001).

24. Dresselhaus, M. S., Dresselhaus, G., Saito, R. & Jorio, A. Raman spectroscopy of carbon nanotubes. *Phys. Rep.* **409,** 47–99 (2005).

25. Ni, Z. H., Wang, Y. Y., Yu, T. & Shen, Z. X. Raman spectroscopy and imaging of graphene. *Nano Res.* **1,** 273–291 (2008).

26. Gupta, A. K, Russin, T. J., Gutiérrez, H. R. & Eklund, P. C. Probing graphene edges via Raman scattering. *ACS Nano* **3,** 45–52 (2009).

27. Lin, Y. M. & Avouris, P. Strong suppression of electrical noise in bilayer graphene nanodevices. *Nano Lett.* **8,** 2119–2125 (2008).

28. Han, M. Y., Brant, J. C. & Kim, P. Electron transport in disordered graphene nanoribbons. *Phys. Rev. Lett.* **104,** 056801 (2010).

29. Liang, W. *et al.* Fabry–Perot interference in a nanotube electronwaveguide. *Nature* **411,** 665–669 (2001).

30. Todd, K., Chou, H. T., Amasha, S. & Goldhaber-Gordon, D. Quantum dot behavior in graphene nanoconstrictions. *Nano Lett* **9,** 416–421 (2009).

Author contributions

H.D. and L.J. conceived and designed the experiments. L.J., X.W., G.D. and H.W. performed the experiments and analysed the data. H.D. and L.J. co-wrote the manuscript. All authors discussed the results and commented on the manuscript.

Facile synthesis of high-quality graphene nanoribbons

Liying Jiao, Xinran Wang, Georgi Diankov, Hailiang Wang and Hongjie Dai

In the version of this Letter originally published, the symbols for 'Lithography (ref. 27)' and 'Sonochemical (ref. 1)' in the legend of Figure 4d were the wrong way round. This error has now been corrected in the HTML and PDF versions of the text.